Available online at www.sciencedirect.com
SCIENCE DIRECT®
Journal of Solid State Chemistry 177 (2004) 972–978
JOURNAL OF SOLID STATE CHEMISTRY
http://elsevier.com/locate/jssc

A TEM study of Ni ordering in the $Ni_6Se_{5-x}Te_x$, $0<x<\sim 1.7$, system

Ray L. Withers,[a,*] Yun Liu, Lasse Norén, and John D. Fitz Gerald[b]

[a] *Research School of Chemistry, Australian National University, GPO Box 4, Canberra ACT 0200, Australia*
[b] *Research School of Earth Sciences, Australian National University, Canberra ACT 0200, Australia*

Received 7 July 2003; received in revised form 24 September 2003; accepted 28 September 2003

Abstract

The $Ni_6Se_{5-x}Te_x$, $0<x<\sim 1.7$, system has been carefully investigated via electron diffraction and TEM imaging. They reveal a somewhat disordered modulated superstructure phase arising from Ni ion ordering within an essentially well-defined chalcogen substructure. As x, and the underlying parent substructure cell dimensions increase, the incommensurate primary modulation wavevector $\mathbf{q}$ characteristic of this Ni ion ordering quickly swings from close to $\frac{1}{2}\mathbf{a}^*$ for $x=0$ towards $\frac{1}{2}[101]^*$ for $x\geqslant 0.5$. A lock-in to $\frac{1}{2}[101]^*$ would formally transform the underlying parent *Bmmb* ($\mathbf{a}_p$, $\mathbf{b}_p$, $\mathbf{c}_p$) structure into a *P*1*a*1 ($\mathbf{a}_s=2\mathbf{a}_p$, $\mathbf{b}_s=\mathbf{b}_p$, $\mathbf{c}_s=-\frac{1}{2}\mathbf{a}_p+\frac{1}{2}\mathbf{c}_p$) superstructure phase.

1. Introduction

Closely related nickel chalcogenide solid solution phases near the nominal composition $Ni_{6\pm x}X_5$ are known to exist for both $X=S$ and $X=Se$ [1–12]. The phases are only thermodynamically stable over a limited temperature interval (400–570°C and 450–670°C for $X=S$ and Se, respectively [5,10]). They can, however, be stabilized to room temperature either via rapid quenching or via doping of S with Se in the case of $Ni_{6\pm x}S_5$ or of Se with Te in the case of $Ni_{6\pm x}Se_5$ [5,6]. In the case of the sulfide, up to four quite distinct metastable phases can apparently be obtained dependent upon the quench rate, or from the as-quenched material via appropriate, surprisingly low temperature heat treatment [10]. In the case of the selenide, only one such phase has to date been reported [11].

The underlying average structure [6,8] in each case is orthorhombic *Bmmb* with similar, although chalcogen size dependent, cell dimensions (e.g. $a_p\sim 3.43$, $b_p\sim 17.06$, $c_p\sim 11.85$ Å for $X=Se$—see Fig. 1). Density measurements suggest that this average structure unit cell always contains 20 chalcogen atoms whereas the number of Ni atoms is able to vary within certain limits around 23–24 per unit cell [1,6,8]. In the asymmetric unit there are three fully occupied chalcogen sites (represented by the largest circles in Fig. 1) and five Ni sites, two of which are essentially fully occupied (represented by the medium sized circles) while three are essentially half occupied (represented by the smallest circles and occurring within the shaded bands of Fig. 1) [6,8]. Open and filled circles represent atoms at heights of $x=0$ and $\frac{1}{2}$, respectively in Fig. 1. Chalcogen atoms at $x=0$ and $\frac{1}{2}$ form zig-zag chains running along the **b** direction. Empty trigonal prisms of chalcogen atoms occur at the turning points of these zig-zag chains while the close by, fully occupied Ni atom sites are in distorted square pyramidal co-ordination environments [6,8]. Half-way between these turning points are $a-c$ planes of half-occupied Ni sites (occurring within the broader gray bands of Fig. 1). The two types of half-occupied Ni atom sites in these regions are in distorted tetrahedral and octahedral co-ordination environments, respectively. Some neighboring Ni sites within this broad gray band are so close together that they cannot be simultaneously occupied (see the encircled Ni atom sites in Fig. 1). There is one remaining half-occupied Ni atom site (occurring within the narrow gray bands of Fig. 1a). This site is again in a distorted tetrahedral environment [8].

Phases of this sort are of interest both because of the apparent ease of Ni diffusion within the chalcogenide sub-structure as well as their concomitant propensity to form complex superstructure phases associated with Ni ordering within the well-defined chalcogenide sub-structure [8,10–12].

*Corresponding author. Fax: +612-612-50750.
E-mail address: withers@rsc.anu.edu.au (R.L. Withers).

0022-4596/$ - see front matter © 2003 Elsevier Inc. All rights reserved.
doi:10.1016/j.jssc.2003.09.042

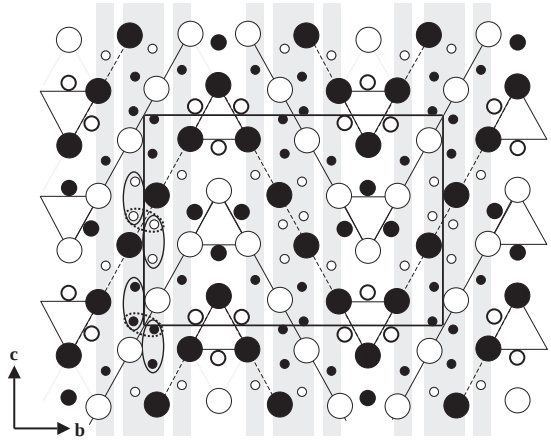

Fig. 1. Shows the refined average structure of Ni_7S_6 [8] projected onto the $b-c$ plane. The chalcogen atoms are depicted by the large circles, the Ni atoms with essentially full occupancy by the medium size circles and the Ni-atoms with $\sim 50\%$ occupancy (occurring within the shaded portions of Fig. 1) by the small circles. Unfilled symbols are at the height $x = 0$ while the filled symbols are at the height $x = \frac{1}{2}$. Some of the $\sim 50\%$ occupied Ni-atoms have been circled in pairs to show that these pairs of Ni atoms have unnaturally short interatomic separation distances and hence can not be simultaneously occupied.

We recently reported on the metastable $Ni_{7\pm x}S_6$ and mixed $Ni_6S_{5-x}Se_x$, phases [12]. Two quite distinct structural polymorphs were identified associated with different patterns of Ni ion ordering. In this paper, we report on the $Ni_6Se_{5-x}Te_x$, $0 < x < \sim 1.7$, system. In the case of the pure selenide end-member, a recent transmission electron microscope (TEM) study of the quenched material found a single, incommensurate (in general) interface modulated, $Ni_{6\pm x}Se_5$ solid solution phase [11] characterized by superspace group symmetry $Pmmn(\frac{1}{2}+\varepsilon, 0, 0)\bar{1}ss$ and incommensurate primary modulation wave-vector $\mathbf{q} = (\frac{1}{2}+\varepsilon)\mathbf{a}^*$ (see Fig. 2 of Ref. [11]). In this paper we report on the existence of a crystallographically distinct incommensurate, interface modulated superstructure phase in the $Ni_6Se_{5-x}Te_x$, $0 < x < \sim 1.7$, system.

2. Experimental

2.1. Synthesis

Ternary compounds $Ni_6Se_{5-x}Te_x$ ($x = 0.1$, 0.5, 1.0 and 1.5) were prepared via solid-state reaction in evacuated and sealed silica tubes. The calculated amounts of high-purity Ni, Se and Te elements were first melted together at 1000°C for 2 h followed by rapid quenching into water. The resultant material was then ground thoroughly in a mortar, pressed into pellets and re-sealed again into evacuated and sealed silica tubes. After being annealed at 570°C for a further 2 days, an X-ray powder pattern was taken. Re-annealing was performed at the same temperature for up to 10 days until the XRD patterns remained unchanged.

2.2. X-ray powder diffraction

The underlying average structure unit cell dimensions of the various samples were determined via XRD using a Guinier–Hägg camera and the program "Unit Cell". Silicon ($a = 5.4310280$ Å at 22.5°C) was used as an internal standard.

3. Results and discussion

3.1. XRD

Single phase $Ni_6Se_{5-x}Te_x$, $x = 0.1$, 0.5, 1.0 and 1.5, specimens were obtained in each case after annealing for an appropriate length of time. The XRD diffraction lines corresponding to the underlying average, or parent, structure of these 4 samples remained quite sharp right across the solid solution field. The relative intensities of some of the lines, however, changed significantly with increasing Te content, e.g. the $\langle 110 \rangle_p^*$ (subscript p for parent here and in what follows) line disappeared altogether for the $x = 1.0$ and 1.5 specimens. The refined metrically orthorhombic, *Bmmb* average structure unit cell dimensions are shown in Table 1. As expected [4,5], the lattice parameters and volume systematically increase with increasing x because of the larger size of Te relative to Se. This increased volume is presumably the driving force for the observed change in the pattern of Ni ion ordering discussed below.

3.2. TEM

Fig. 2 shows (a) $[001]_p$, (b) $[010]_p$, (c) $[100]_p$ and (d) $\langle 2\bar{1}0 \rangle_p$ zone axis electron diffraction patterns (EDPs) typical of the somewhat disordered $x = 0.1$ specimen, the composition closest to the Ni_6Se_5 end-member. Integer indexation of the incommensurate EDPs in Fig. 2 is with respect to the four basis vectors $M = \{\mathbf{a}_p^*, \mathbf{b}_p^*, \mathbf{c}_p^*, \mathbf{q} = (\frac{1}{2}+\varepsilon)\mathbf{a}_p^* + \psi\mathbf{c}_p^*\}$. The parameter ε, while small and clearly non-zero, is nonetheless well-defined. The parameter $\psi \sim 0.1 \pm 0.1$, however, is not so well-defined

Table 1
Refined underlying average structure unit cell parameters for $Ni_6Se_{5-x}Te_x$ ($0 < x \leqslant \sim 1.7$) compounds

x	a_p (Å)	b_p (Å)	c_p (Å)	V (Å^3)
0.1	3.4387(8)	17.094(3)	11.854(3)	1393.6(5)
0.5	3.4643(4)	17.136(1)	11.921(1)	1415.4(2)
1.0	3.4915(4)	17.162(2)	11.989(1)	1436.9(3)
1.5	3.5225(4)	17.173(2)	12.013(2)	1453.4(4)

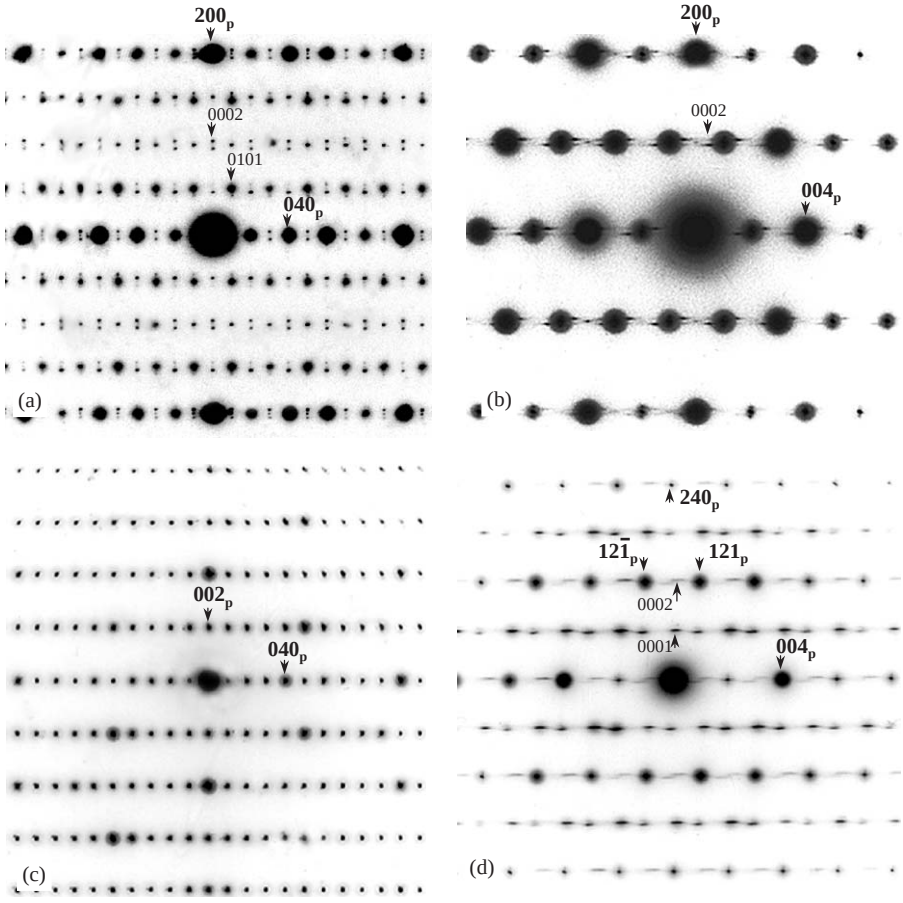

Fig. 2. (a) $[001]_p$, (b) $[010]_p$, (c) $[100]_p$ and (d) $\langle 2\bar{1}0\rangle_p$ zone axis EDPs typical of the somewhat disordered $x = 0.1$ specimen, the composition closest to the Ni_6Se_5 end-member. Four-integer indexation of the incommensurate EDPs is with respect to the four basis vectors $M = \{\mathbf{a}_p^*, \mathbf{b}_p^*, \mathbf{c}_p^*, \mathbf{q} = (\frac{1}{2} + \varepsilon)\mathbf{a}_p^* + \psi\mathbf{c}_p^*\}$. Three-index notation with the subscript p is with espect to the underlying *Bmmb* ($\mathbf{a}_p$, $\mathbf{b}_p$, $\mathbf{c}_p$) parent structure (see Fig. 1).

(cf. Figs. 2b with a) leading to the observed marked smearing of the satellite reflections along the $\mathbf{c}_p^*$ direction. In projection along $\mathbf{c}_p$ (see Fig. 2a), such smearing is of course masked. The $[001]_p$ zone axis EDP of this $x = 0.1$ specimen thus appears very similar to, if not identical with, the equivalent $[001]_p$ zone axis EDP of the Ni_6Se_5, $x = 0$, end-member (cf. Fig. 2a with Fig. 2a of Ref. [11]). The differences in their reciprocal lattices are more apparent in the respective $[010]_p$ zone axis EDPs (cf. Fig. 2b with Fig. 2b of Ref. [11]). In particular, the primary modulation wave-vector $\mathbf{q}$, in the case of the $x = 0.1$ specimen, has clearly swung from very close to $\frac{1}{2}\mathbf{a}_p^*$ for $x = 0$ towards $\frac{1}{2}[101]_p^*$ (see, e.g. Fig. 2d). On the other hand, the absence of $[h0lm]^*$ satellite reflections unless m is even in both $[010]_p$ zone axis EDPs is a point of similarity between the two reciprocal lattices and requires the existence of an $\{x_1, -x_2 + \frac{1}{2}, x_3, x_4 + \frac{1}{2}\}$ superspace hyper-glide plane perpendicular to $\mathbf{b}_p$.

That the absence of $[h0lm]^*$, m odd, satellite reflections in Fig. 2b is a genuine extinction condition is apparent from the presence of m odd satellite reflections in the $\langle 210\rangle_p$ zone axis EDP of Fig. 2d. Fig. 2d also shows that the 'swinging' primary modulation wave-vector has formally lowered the overall superspace group symmetry to monoclinic and only pseudo-orthorhombic, i.e. the original *mmm* Laue symmetry of the *Bmmb* average structure has been reduced to $12/m1$ and clearly no longer includes mirror planes perpendicular to $\mathbf{c}_p^*$ or $\mathbf{a}_p^*$. As should be expected, this commonly leads to twinning perpendicular to $\mathbf{c}_p^*$, as is apparent in, e.g. Figs. 2b and 3d (see also Fig. 4).

Increasing x lead to rapid further swinging of the primary modulation wave-vector $\mathbf{q}$ towards $\frac{1}{2}[101]_p^*$ (see, for example, the absence of satellite reflections in the $[001]_p$ zone axis EDP of Fig. 3a and more directly in Figs. 3c and d). Fig. 3 shows (a) $[001]_p$, (b) $[010]_p$, (c) $\langle 30\bar{1}\rangle_p$ and (d) $\langle 2\bar{1}0\rangle_p$ zone axis EDPs of the $x = 0.5$ specimen but also in fact typical of both the $x = 1.0$ and 1.5 specimens. In some grains, apparently discrete incommensurate satellite reflections on either side of the $\mathbf{G}_p \pm \frac{1}{2}[101]_p^*$ positions of reciprocal space ($\mathbf{G}_p$ refers to the set of parent Bragg reflections) occur while in others these apparently discrete satellite reflections blur together somewhat more to form a series of reciprocal space 'dashes' running essentially along $\mathbf{c}_p^*$ but centered

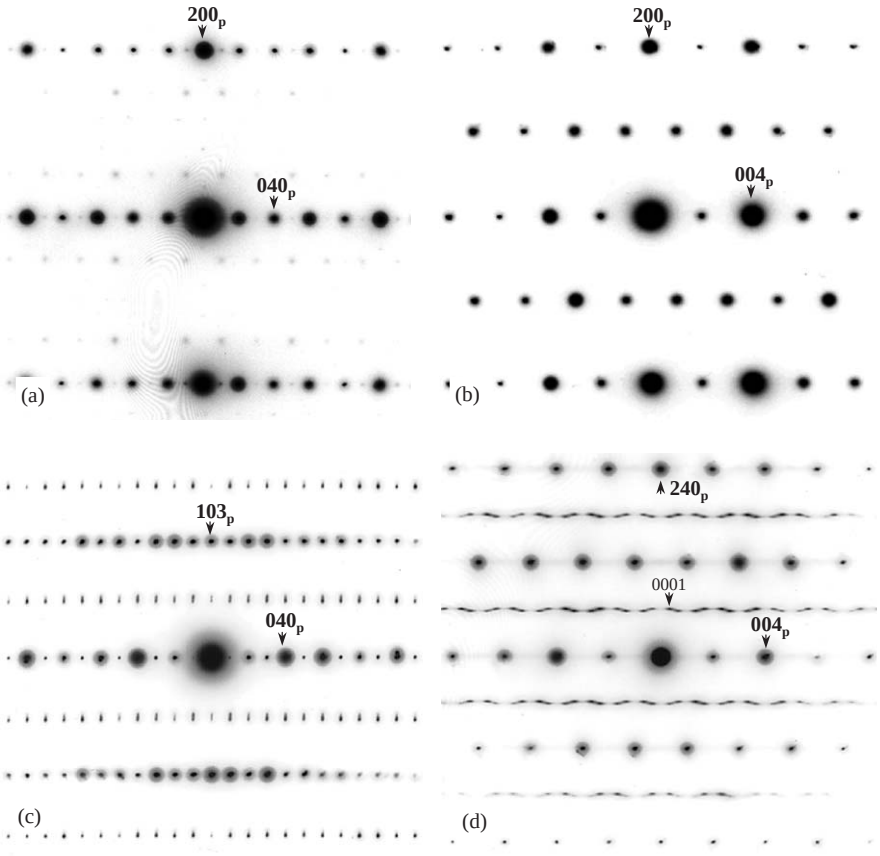

Fig. 3. (a) $[001]_p$, (b) $[010]_p$, (c) $\langle 30\bar{1}\rangle_p$ and (d) $\langle 2\bar{1}0\rangle_p$ zone axis EDPs of the $x = 0.5$ specimen. Integer indexation of the incommensurate EDPs is with respect to the four basis vectors $M = \{\mathbf{a}_p^*, \mathbf{b}_p^*, \mathbf{c}_p^*, \mathbf{q} = (\frac{1}{2} + \varepsilon)\,\mathbf{a}_p^* + \psi\mathbf{c}_p^*\}$. Three-index notation with the subscript p is with respect to the underlying *Bmmb* ($\mathbf{a}_p$, $\mathbf{b}_p$, $\mathbf{c}_p$) parent structure (see Fig. 1).

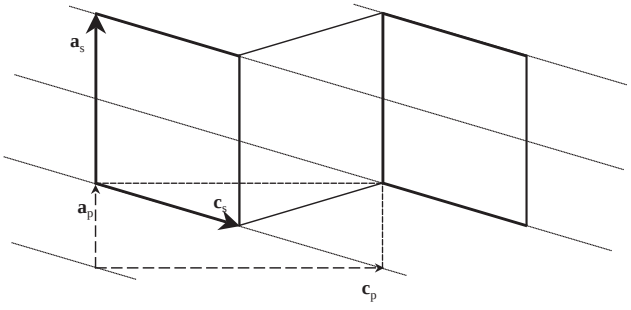

Fig. 4. Shows a drawing of the resultant $\mathbf{a}_s = 2\mathbf{a}_p$, $\mathbf{b}_s = \mathbf{b}_p$, $\mathbf{c}_s = -\frac{1}{2}\mathbf{a}_p + \frac{1}{2}\mathbf{c}_p$ supercell) projected along the unique $\mathbf{b}_s = \mathbf{b}_p$ orientation (represented by the heavy dark lines). One twin variant of this supercell is also shown (in a lighter line) along with the $\frac{1}{2}\mathbf{a}_s = \mathbf{a}_p$ offset (see the $[10\bar{1}]_p$ dashed lines) which can arise as a result of micro-twinning, i.e. twinning followed almost immediately by a further twin back to the original twin orientation. The parent $\mathbf{a}_p$ and $\mathbf{c}_p$ cell vectors are also shown.

on the $\mathbf{G}_p \pm \frac{1}{2}[101]_p^*$ positions of reciprocal space. Like the $x = 0.1$ specimen, the absence of $[h0lm]^*$, $m = 1$, satellite reflections at the $[010]_p$ zone axis orientation implies the presence of an $\{x_1, -x_2 + \frac{1}{2}, x_3, x_4 + \frac{1}{2}\}$ superspace hyper-glide plane perpendicular to $[010]_p$.

The EDPs of all the specimens examined were, in general, always incommensurate although also somewhat disordered as shown in Figs. 2 and 3. Characteristic extinction conditions could nonetheless clearly be identified as follows: $F(hklm) = 0$ unless $h + l$ is even and $F(h0lm) = 0$ unless m is even (see Figs. 2b and 3b). The implied superspace group symmetry is thus at least $B1m1$ $(\frac{1}{2} + \varepsilon, 0, \frac{1}{2} - \gamma)s$ but most probably $B12/m1(\frac{1}{2} + \varepsilon, 0, \frac{1}{2} - \gamma)\bar{1}s$. The corresponding superspace generating operations can be taken to be $\{x_1 + \frac{1}{2}, x_2, x_3 + \frac{1}{2}, x_4\}$, $\{x_1, -x_2 + \frac{1}{2}, x_3, x_4 + \frac{1}{2}\}$ and $\{-x_1, -x_2, -x_3, -x_4 + 2\phi\}$ respectively. The resultant conventional space group symmetry if $\mathbf{q}$ were to lock in to $\frac{1}{2}[101]_p^*$ is therefore formally $P12_1/a1$ ($\mathbf{a}_s = 2\mathbf{a}_p$, $\mathbf{b}_s = \mathbf{b}_p$, $\mathbf{c}_s = -\frac{1}{2}\mathbf{a}_p + \frac{1}{2}\mathbf{c}_p$) if the global phase parameter $\phi = J/4$ (J an integer) and $P1a1$ otherwise. Note, however, that the two inversion related, ~half-occupied Ni sites on either side of the origin (and circled by the dashed lines in Fig. 1b) can never be simultaneously occupied, i.e. a resultant inversion center is not possible. The resultant superstructure space group symmetry can thus only be $P1a1$.

Fig. 4 shows a drawing of this resultant supercell projected along the unique $\mathbf{b}_s = \mathbf{b}_p$ orientation

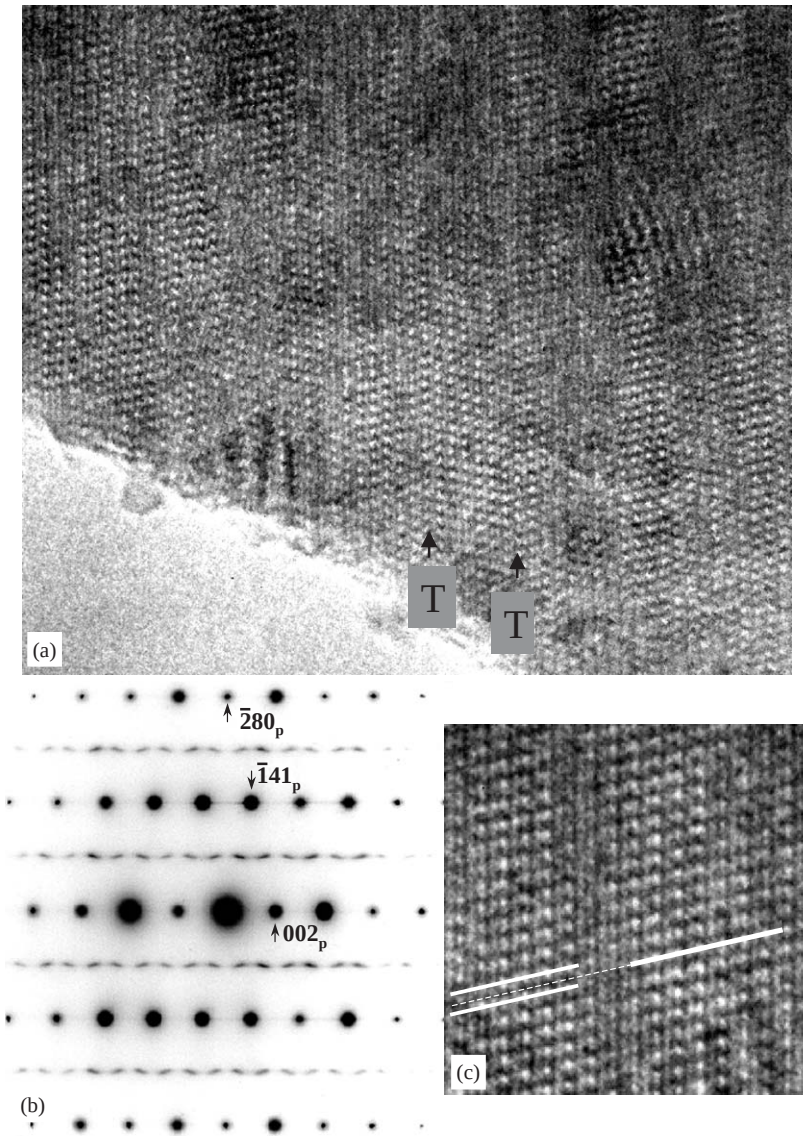

Fig. 5. (a) Shows a real space lattice image taken along [410] (the corresponding EDP aligned appropriately is shown in (b)). Note an oblique pattern of white dots with a unit mesh size of 5.96 Å × 5.26 Å corresponding to the $\mathbf{a}_s = 2\mathbf{a}_p$, $\mathbf{b}_s = \mathbf{b}_p$, $\mathbf{c}_s = -\frac{1}{2}\mathbf{a}_p + \frac{1}{2}\mathbf{c}_p$ superstructure unit cell projected along the $\langle 410 \rangle$ direction as well as the twinned variant thereof intermixed on a relatively fine scale. One such domain in twin orientation, elongated approximately parallel to (001), is denoted by the letters T–T. (c) shows a blow-up of another portion of (a) to emphasize the one-half superfringe displacement (highlighted by the white lines) between neighboring superlattice domains. This can be described as consistent with the presence of an ~(001) APB with a displacement vector $\frac{1}{2}\mathbf{a}_s$. Many similar features exist in this and other recorded images.

(represented by the heavy dark lines). The effect of twinning of this supercell clearly needs to be taken into consideration given the diffraction evidence for such twinning described above in conjunction with the earlier evidence for fine-scale twinning perpendicular to $\mathbf{c}_p$ of a related superstructure phase in the $Ni_{6\pm x}S_5$ phase [12]. One twin variant of the supercell is thus also shown in Fig. 4 along with the $\frac{1}{2}\mathbf{a}_s = \mathbf{a}_p$ offset, which arises if the microtwin thickness is an odd number of supercells thick (clearly the case shown is one supercell thick). Such micro-twinning then is equivalent to a translation defect (or anti-phase boundary, APB) characterized by the displacement vector $\mathbf{R} = \frac{1}{2}\mathbf{a}_s = \mathbf{a}_p$.

Direct evidence for translation defects (see, e.g. Fig. 5c) as well as for the existence of superstructure twin domains (elongated along ~(001)—as in the region T–T in Fig. 5a) can be found in the $\langle 410 \rangle_p$ zone axis EDP and corresponding lattice image of an $x = 0.5$ specimen shown in Fig. 5. (Unfortunately, superlattice twins cannot be imaged along $[010]_p$ since the relevant $\mathbf{G}_p \pm \frac{1}{2}\langle 101 \rangle_p^*$ superlattice reflections are systematically absent at this orientation—see Fig. 3b. It is therefore necessary to image along relatively minor axes). The simultaneous presence of $\mathbf{G}_p \pm \frac{1}{2}[\bar{1}41]_p^*$ and $\mathbf{G}_p \pm \frac{1}{2}[\bar{1}4\bar{1}]_p^*$ satellite reflections in Fig. 5b requires coexistence of the $\mathbf{a}_s = 2\mathbf{a}_p$, $\mathbf{b}_s = \mathbf{b}_p$, $\mathbf{c}_s = -\frac{1}{2}\mathbf{a}_p + \frac{1}{2}\mathbf{c}_p$ superstructure with its

$\mathbf{a}_s = 2\mathbf{a}_p$, $\mathbf{b}_s = \mathbf{b}_p$, $\mathbf{c}_s = +\frac{1}{2}\mathbf{a}_p + \frac{1}{2}\mathbf{c}_p$twin equivalent within the area illuminated to form the EDP. Inspection of the corresponding lattice image indeed shows spatially separated oblique patterns of white dots corresponding to both of these supercells projected along the $\langle 410 \rangle$ direction.

Note that the superstructure twin domains in Fig. 5a are typically elongated parallel to (001) and that it is difficult to judge exactly how many supercells thick they are. Detail from a domain boundary in another part of this field, however, is enlarged in Fig 5c and clearly shows the one half-fringe, APB-like displacement of the $\frac{1}{2}(\bar{1}4\bar{1})^*_p$-oriented superlattice between neighboring domains. Similar APB features have commonly been imaged along other crystal directions, such as $\langle 10\bar{1} \rangle_p$ (where only one of the twin superlattice domains was imaged and the (001) domain boundaries were inclined to the viewing direction).

If wide twin domains were present, only sharp $\mathbf{G}_p \pm \frac{1}{2}[\bar{1}41]^*_p$ and $\mathbf{G}_p \pm \frac{1}{2}[\bar{1}4\bar{1}]^*_p$ satellite reflections would be observed in Fig. 5b. The streaking (or 'incommensurate splitting') of the satellite reflections on either side of the $\mathbf{G}_p \pm \frac{1}{2}\langle \bar{1}01 \rangle^*_p$ positions of reciprocal space (generally in the $\mathbf{c}^*_p$ direction) as seen in Fig. 5b clearly results from the existence of narrow (001) superlattice domains irregular in shape and size but characterized by planar translation defects or APBs. This feature is like that reported in Ref. [13] where the separation of defects was also concluded to be inversely proportional to the splitting of the reflections. A perfectly regularly spaced sequence of such APBs could split the $G_p \pm (1/2)[101]^*_p$ satellite reflections in the $\mathbf{c}^*_p$ direction and give rise to sharp incommensurate satellite reflections. In practice, however, the observed lack of regularity in this spacing explains the blurry character of the observed satellite reflections (see Fig. 5b).

A (partial) model for the Ni atom ordering presumed responsible for the local $P1a1$ ($\mathbf{a}_s = 2\mathbf{a}_p$, $\mathbf{b}_s = \mathbf{b}_p$, $\mathbf{c}_s = -\frac{1}{2}\mathbf{a}_p + \frac{1}{2}\mathbf{c}_p$) superstructure and compatible with the observed TEM evidence is shown in projection down the resultant $\mathbf{a}_s = 2\mathbf{a}_p$ direction in Fig. 6. The projected supercell along the $\mathbf{a}_s$ orientation is represented by the heavy dark lines while the projected average structure unit cell is represented by the dashed lines (cf. with Fig. 4). A 1 in Fig. 6 represents an occupied site while a 0 represents an empty site. The doubled ($\mathbf{a}_s = 2\mathbf{a}_p$) repeat along the parent $\mathbf{a}_p$ direction means that two numbers are required for each projected site in order to specify the Ni atom distribution. These two numbers are given for each projected site in between the round brackets. In the case of the open circles these Ni atom heights are at $x = 0$ and 1, respectively (with respect to the parent structure, see Fig. 1) while for the filled circles these Ni atom heights are at $x = \frac{1}{2}$ and $\frac{3}{2}$, respectively. No attempt has been made to order the occupancies of the other half-occupied Ni atom site (within the narrow gray bands of Fig. 6) as we have no information (from either crystal chemical or symmetry considerations) as to how the occupancy of this site might correlate with the occupancies of the other Ni atom sites. Further progress will require some sort of structure refinement. Given the extent of disorder revealed by the current TEM study, as manifested in the streaking of the observed satellite reflections, such a refinement is currently not a viable option.

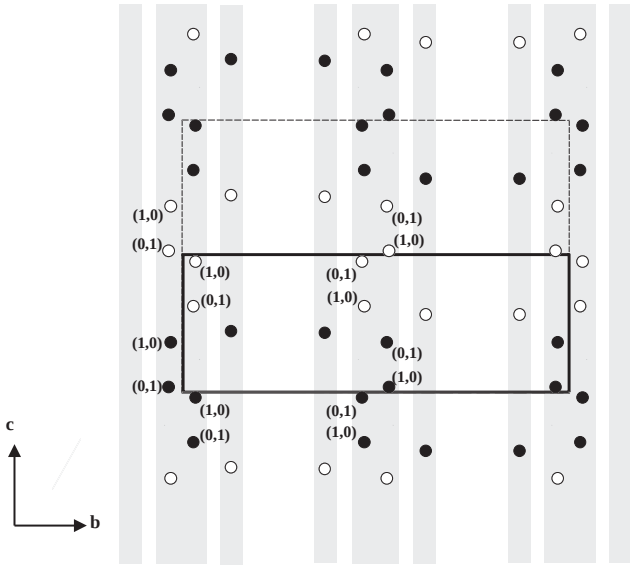

Fig. 6. A (partial) model for the Ni atom ordering responsible for the local $P1a1$ ($\mathbf{a}_s = 2\mathbf{a}_p$, $\mathbf{b}_s = \mathbf{b}_p$, $\mathbf{c}_s = -\frac{1}{2}\mathbf{a}_p + \frac{1}{2}\mathbf{c}_p$) superstructure in projection down the resultant $\mathbf{a}_s = 2\mathbf{a}_p$ direction. The projected supercell along the $\mathbf{a}_s$ orientation is represented by the heavy dark lines while the projected average structure unit cell is represented by the dashed lines (cf. with Fig. 4). A 1 in Fig. 6 represents an occupied site while a 0 represents an empty site. The doubled ($\mathbf{a}_s = 2\mathbf{a}_p$) repeat along the parent $\mathbf{a}_p$ direction means that two numbers are required for each projected site in order to specify the Ni atom distribution. These two numbers are given for each projected site in between the round brackets. In the case of the open circles these Ni atom heights are at $x = 0$ and 1, respectively (with respect to the parent structure, see Fig. 1) while for the filled circles these Ni atom heights are at $x = \frac{1}{2}$ and $\frac{3}{2}$, respectively.

4. Conclusions

It would appear that the expansion of the underlying *Bmmb* ($\mathbf{a}_p$, $\mathbf{b}_p$, $\mathbf{c}_p$) parent unit cell associated with the substitution of the larger Te ion for the Se ion creates more space for the Ni ions and allows for the condensation of yet another distinct pattern of incommensurate Ni ion ordering within an essentially well-defined chalcogen sub-structure. Incommensurability in the $Ni_6Se_{5-x}Te_x$, $0 < x < \sim 1.7$ solid solution is associated with the introduction into a $P1a1$ ($\mathbf{a}_s = 2\mathbf{a}_p$, $\mathbf{b}_s = \mathbf{b}_p$, $\mathbf{c}_s = -\frac{1}{2}\mathbf{a}_p + \frac{1}{2}\mathbf{c}_p$) superstructure (see Fig. 6) of variably spaced, non-conservative $\sim$(001) APBs. The

observed lack of perfect regularity in the spacing of these APBs might well be affected by strain induced by variability in the local Se/Te distribution on the chalcogenide sub-structure. The existence of yet another distinct pattern of Ni ion ordering within the same well-defined, albeit slightly expanded, chalcogenide sub-structure illustrates yet again the remarkable variety of Ni ion arrangement in this family of closely related superstructure phases.

Acknowledgments

Two of the authors (RLW and YL) gratefully acknowledge the Australian Research Council (ARC) for financial support in the form of an ARC Discovery Grant.

References

[1] T.B. Massalski (Ed.), Binary Alloy Phase Diagrams, American Society for Metals, Metals Park, OH, 1986.
[2] F. Grønvold, R. Møllerud, E. Røst, Acta Chem. Scand. 20 (1966) 1997.
[3] H. Haraldsen, R. Møllerud, E. Røst, Acta Chem. Scand. 21 (1967) 1727.
[4] E. Røst, E. Vestersjø, Acta Chem. Scand. 22 (1968) 2118.
[5] A.L.N. Stevels, Philips Res. Rep. (9) (1969) 124.
[6] K. Haugsten, E. Røst, Acta Chem. Scand. 23 (1969) 3599.
[7] E. Røst, K. Haugsten, Acta Chem. Scand. 25 (1971) 3194.
[8] M.E. Fleet, Acta Crystallogr. B 28 (1972) 1237.
[9] G. Åkesson, E. Røst, Acta Chem. Scand. A 29 (1975) 236.
[10] H. Seim, H. Fjellvåg, F. Grønvold, S. Stølen, J. Solid State Chem. 121 (1996) 400.
[11] L. Norén, G. van Tendeloo, R.L. Withers, J. Solid State Chem. 162 (2001) 122.
[12] Y. Liu, L. Norén, R.L. Withers, J. Hadermann, G. van Tendeloo, F.J. Gárcia-Gárcia, J. Solid State Chem. 170 (2003) 351.
[13] J. Van Landuyt, R. De Ridder, R. Gevers, S. Amelinckx, Mater. Res. Bull. 5 (1970) 353.